

REPORT DOCUMENTATION PAGE				Form Approved OMB No. 0704-0188	
<p>Public reporting burden for this collection of information is estimated to average 1 hour per response, including the time for reviewing instructions, searching existing data sources, gathering and maintaining the data needed, and completing and reviewing this collection of information. Send comments regarding this burden estimate or any other aspect of this collection of information, including suggestions for reducing this burden to Department of Defense, Washington Headquarters Services, Directorate for Information Operations and Reports (0704-0188), 1215 Jefferson Davis Highway, Suite 1204, Arlington, VA 22202-4302. Respondents should be aware that notwithstanding any other provision of law, no person shall be subject to any penalty for failing to comply with a collection of information if it does not display a currently valid OMB control number. PLEASE DO NOT RETURN YOUR FORM TO THE ABOVE ADDRESS.</p>					
1. REPORT DATE (DD-MM-YYYY) July 2012		2. REPORT TYPE Journal Article		3. DATES COVERED (From - To) July 2012- July 2012	
4. TITLE AND SUBTITLE Effects of Peripheral Architecture on the Properties of Aryl Polyhedral				5a. CONTRACT NUMBER IN-HOUSE	
				5b. GRANT NUMBER	
				5c. PROGRAM ELEMENT NUMBER	
6. AUTHOR(S) Gregory R. Yandek, Brian M. Moore, Sean M. Ramirez, Joseph M. Mabry				5d. PROJECT NUMBER	
				5e. TASK NUMBER	
				5f. WORK UNIT NUMBER Q0AD	
7. PERFORMING ORGANIZATION NAME(S) AND ADDRESS(ES) Air Force Research Laboratory (AFMC) AFRL/RZSM 9 Antares Rd. Edwards AFB, CA, 93524-7401				8. PERFORMING ORGANIZATION REPORT NO.	
9. SPONSORING / MONITORING AGENCY NAME(S) AND ADDRESS(ES) Air Force Research Laboratory (AFMC) AFRL/RQR 5 Pollux Dr. Edwards AFB, CA, 93524-7048				10. SPONSOR/MONITOR'S ACRONYM(S)	
				11. SPONSOR/MONITOR'S REPORT NUMBER(S) AFRL-RQ-ED-JA-2012-246	
12. DISTRIBUTION / AVAILABILITY STATEMENT Approved for public release; distribution unlimited					
13. SUPPLEMENTARY NOTES Journal article published in the Journal of Physical Chemistry Vol. #116, Issue #31, July 2012. PA Case Number: #12644; Clearance Date: 30 July 2012. © 2012 American Chemical Society The U.S. Government is joint author of the work and has the right to use, modify, reproduce, release, perform, display, or disclose the work.					
14. ABSTRACT The effects of the peripheral architecture on the macroscopic properties of eight symmetric and asymmetric aryl polyhedral oligomeric silsesquioxane (POSS) molecules are described. These POSS materials were synthesized in our laboratory and characterized by single-crystal and powder Xray diffraction techniques, as well as differential scanning calorimetry, thermogravimetric analysis, mass spectrometry, and Fourier transform infrared spectroscopy. The peripheral aryl architecture, although similar in most cases, was found to significantly influence observed thermally induced phase transitions, mass loss during decomposition, and heat capacity. These properties are correlated to POSS assembly, molecular interactions, and the specific attributes of peripheral structure and connectivity to the inorganic core.					
15. SUBJECT TERMS					
16. SECURITY CLASSIFICATION OF:			17. LIMITATION OF ABSTRACT	18. NUMBER OF PAGES	19a. NAME OF RESPONSIBLE PERSON
a. REPORT	b. ABSTRACT	c. THIS PAGE			Joseph Mabry
Unclassified	Unclassified	Unclassified	SAR	12	19b. TELEPHONE NO (include area code) 661-275-5857

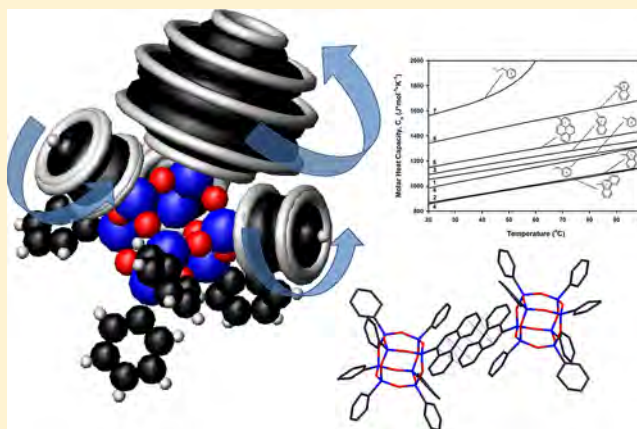
Effects of Peripheral Architecture on the Properties of Aryl Polyhedral Oligomeric Silsesquioxanes

Gregory R. Yandek,^{*,†} Brian M. Moore,[†] Sean M. Ramirez,[‡] and Joseph M. Mabry^{*,†}

[†]Rocket Propulsion Division, Air Force Research Laboratory, Edwards AFB, California 93524, United States

[‡]Rocket Propulsion Division, Air Force Research Laboratory, ERC, Inc., Edwards AFB, California 93524, United States

ABSTRACT: The effects of the peripheral architecture on the macroscopic properties of eight symmetric and asymmetric aryl polyhedral oligomeric silsesquioxane (POSS) molecules are described. These POSS materials were synthesized in our laboratory and characterized by single-crystal and powder X-ray diffraction techniques, as well as differential scanning calorimetry, thermogravimetric analysis, mass spectrometry, and Fourier transform infrared spectroscopy. The peripheral aryl architecture, although similar in most cases, was found to significantly influence observed thermally induced phase transitions, mass loss during decomposition, and heat capacity. These properties are correlated to POSS assembly, molecular interactions, and the specific attributes of peripheral structure and connectivity to the inorganic core.



INTRODUCTION

Polyhedral oligomeric silsesquioxanes (POSS¹) have influenced a spectrum of applications^{2–12} due to their hybridized organic and inorganic character as well as a unique versatility in their synthesis, providing diversity in molecular structures. Such diversity is rooted in the flexibility to manipulate the organic periphery and the size of the POSS core, where specific tuning for a particular application can be accomplished. The organic periphery is known to affect POSS dispersion in host materials, which dictates delivered composite properties.^{13,14} For the purpose of fabricating polymer nanocomposites (PNCs), the periphery may be designed to interact with the polymer host, either covalently or noncovalently. Dispersion of POSS in PNCs is generally best achieved when POSS is either covalently bound to the polymer or there is an alternative form of interaction,¹⁵ particularly when the periphery is electronically similar to the polymer host.^{13,16} The size of the organic periphery also plays a role in dispersion, especially when the host polymer is nonpolar, where larger organic groups mitigate unfavorable interactions between the host and the hydrophilic inorganic core.^{17,18}

In terms of the relationship between POSS structure and macroscopic properties, the nature of the organic periphery has been observed to affect molecular packing, phase transitions, and thermal properties. In general, POSS molecules are inherently thermally stable and are often utilized to improve the temperature robustness of polymer hosts. However, relatively few reports address the intrinsic thermal stability of individual POSS compounds and the effect of structure on degradation mechanisms.^{19–22} Notably, Fina et al. demonstrated through thermogravimetric analysis (TGA) experiments

that the POSS periphery plays a significant role in thermal stability; that is, aromatic moieties impart superior stability to those that are aliphatic, attributing the contrasting behaviors to the intrinsic stabilities of these organic groups.¹⁹ Specifically, POSS molecules featuring an aliphatic periphery were shown to volatilize as a function of molecular weight, independent of atmosphere, at temperatures between 150 and 350 °C, leaving little ultimate residue. Aryl-functionalized POSS compounds, on the other hand, have been shown to be thermally stable in excess of 350 °C, leaving substantial residue in nitrogen, suggesting that chemical degradation is the dominant mass loss mechanism. From the perspective of bond strengths, the Si–C bond, which universally links the Si atoms to the organic corona, is reported to possess a similar value to that of the C–C bond.^{23,24} Therefore, the contrasting thermally induced mass loss behaviors of aliphatic and aryl POSS cannot be solely explained by quantitative bond disassociation energies, suggesting that thermal stability may also be dependent on molecular assembly, characterized by packing density, binding energy, interperiphery interactions, and solid–liquid phase transitions. In the present case, the high melting point of aryl POSS may be significantly attributed to aromatic interactions according to van der Waals bonding between phenyl groups.

In terms of the specific application of utilizing inert POSS molecules as additives in polymer hosts, aliphatic varieties (i.e., octamethyl, octaisooctyl, octaisobutyl, and octacyclohexyl) have been shown to act as plasticizers, heterogeneous crystallization

Received: April 24, 2012

Revised: June 29, 2012

Published: July 26, 2012



nucleation sites,^{17,25} toughening agents,²⁶ and thermal stability promoters in thermoplastic olefins.²⁷ Similar successes have not been achieved in high temperature, aromatic engineering thermoplastic hosts using nonreactive aryl POSS compounds, such as octaphenyl and dodecaphenyl POSS. These molecules, unlike their aliphatic counterparts with reasonably low melting points, exist as crystalline powders, ranging in particle size from 1 to 100 μm . Their crystals possess high binding energies, resulting in melt transitions at temperatures in the vicinity where degradation transpires, thus compromising the use of melt blending techniques. These types of POSS are also resistant to solvation by low molecular weight liquids. Because of these characteristics, effective dispersion of these compounds has proven difficult. Recently, we reported four new aryl POSS compounds that are peripherally asymmetric to circumvent this shortcoming.²⁸ These compounds demonstrate enhanced solubility and high temperature polymer miscibility characteristics, without sacrificing absolute peripheral aromaticity. The effects of aryl architecture on the bulk properties of these compounds and other previously reported aryl POSS materials are not completely understood. This work seeks to unveil correlations between the peripheral framework of inert aryl POSS molecules, assembly and packing efficiency, and thermal properties, for the purposes of advancing the efficiency of molecular design and the fabrication of high performance PNCs as well as other applications.

EXPERIMENTAL DESCRIPTION

Materials. Phenyl₇Si₇O₉(OH)₃ was obtained from Hybrid Plastics, while additional silicon-containing organic compounds were purchased from Gelest. All remaining chemicals were purchased from Aldrich. Chemicals were used without further purification unless otherwise noted. All reactions were performed under an atmosphere of dry nitrogen. Flasks were oven-dried and allowed to cool under nitrogen prior to use. The procedures used to synthesize all trichlorosilanes used in this study are reported in our previous work.²⁸ Octabenzyl POSS²³ (6) was synthesized according to a previously published method consisting of the hydrolytic condensation of benzyl trichlorosilane.²⁹ Octaphenethyl POSS (7) was synthesized through the pressurized hydrogenation of octastyr- enyl POSS using palladium on carbon as the catalyst. Octa(1-naphthyl) POSS (8) was synthesized using a published literature method from 1-naphthyltrichlorosilane starting material.³⁰

Synthesis of Aryl POSS Compounds. POSS compounds 1–5 were synthesized by the “corner-capping” of Ph₇Si₇O₉(OH)₃ with aryl-trichlorosilanes (Figure 1).²⁸ In general, under a dry nitrogen atmosphere, Ph₇Si₇O₉(OH)₃ (19.7 g, 0.021 mol) was dissolved in THF (150 mL). To this, a solution of R-trichlorosilane (5.6 g, 0.022 mol) in THF (50 mL) was added slowly, where R = phenyl (1), 1-naphthyl (2), 2-naphthyl (3), 9-phenanthrenyl (4), and 1-pyrenyl (5). To this mixture, a dilute triethylamine (6.8 g, 0.068 mol) solution in THF (100 mL) was added over a 90 min period under vigorous stirring, and the reaction was allowed to proceed overnight. The solution was then filtered, and the volume was reduced under dynamic vacuum. Ether was then added, and an aqueous workup was performed. The solution was again reduced under vacuum, and the remaining oil was dissolved in THF. The solution was precipitated in methanol and then filtered.

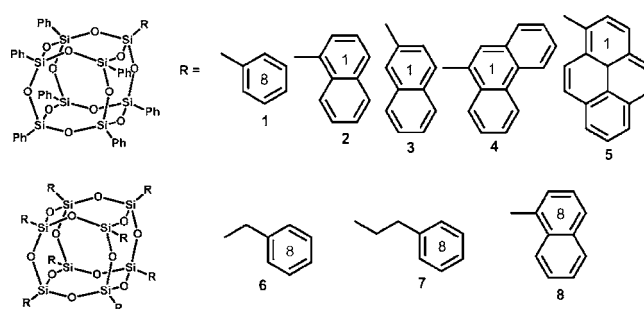


Figure 1. Chemical structures and numbering assignments for the aryl POSS molecules used in this study. The numbers 1 or 8 located within each aryl group indicate the quantity of that group in the peripheral architecture of the designated molecule. Eight denotes symmetry, while 1 represents asymmetry with the variant aryl moiety R shown (the other seven groups in the periphery are phenyls).

The chemical structures of POSS compounds 1–8 are shown in Figure 1 for reference. In the remaining text, these compounds will be referred to by their assigned numbers.

POSS Structural and Chemical Analyses. Purity, structural integrity, and elemental assays were determined by nuclear magnetic resonance (NMR) spectroscopy, combustion analysis, and single-crystal or powder X-ray diffraction (XRD), where applicable. ¹H, ¹³C, and ²⁹Si NMR spectra were obtained on Bruker 300 and 400 MHz spectrometers using 5 mm o.d. tubes. Sample concentrations were approximately 10% (w/v) in CDCl₃ and were referenced to internal solvent. A 15 s delay was used to acquire ²⁹Si NMR spectra. Combustion analysis was performed by Atlantic Microlab, Inc. For XRD, powder samples were loaded into 1 mm diameter quartz capillary tube (Mark-Röhrchen) for measurement. Powder diffraction for each compound was collected at *T* = 298.0 (K) using a Kusing Bruker 3-circle, SMARTAPEX CCD with the *c*-axis fixed at 54.748, running on SMART V 5.625 program (Bruker AXS: Madison, 2001). Graphite monochromated Cu K α (λ = 1.54179 Å) radiation was employed for data collection, which was analyzed using XRD2 Eval (Bruker APEX 2).

POSS Thermal Analyses. TGA was performed using a TA Instruments Q5000 under nitrogen and air atmospheres at a purge rate of 25 mL/min and variable temperature scan rates from ambient depending on experiment type. In general, 3 mg of each sample was tested in platinum pans. In some cases, a Pfeiffer Vacuum ThermoStar Gas Analysis System was utilized to facilitate mass spectrometry of the gaseous byproducts from TGA. The system consists of a heated (170 °C) quartz capillary interfaced with the Q5000 chamber, which in turn is connected to the ThermoStar. A vacuum system pulls the gaseous decomposition byproducts through an ionization source, where electron bombardment occurs, followed by ion separation through the quadrupole mass filter, ultimately undergoing analysis by the ion detection system. Bargraph cycle scans ran for all of the experiments consisting of a repeating detector sweep of *m/z* in the range of 1–199 amu. Customized software was used to analyze the bargraph cycle scan data. Non-isothermal standard differential scanning calorimetry (DSC) was performed on a TA Instruments Q200 coupled with an RCS90 refrigeration cooling system under a nitrogen purge of 50 mL/min and a scan rate of 10 °C/min. Standard aluminum pans were employed containing 5 mg of sample and an empty reference for each experiment. Reversing and nonreversing heat flows were decoupled using modulated differential scanning

calorimetry (MDSC) on the Q200 instrument. For this technique, standard aluminum Tzero pans were utilized containing 10 mg of sample and an empty reference. Because conductivity through the sample from the DSC cell surface is affected by porosity, the powders were compressed in their respective pans to achieve consolidation. The sample was initially equilibrated at 0 °C. Subsequently, the temperature was modulated at amplitude of 1 °C and a period of 100 s. During modulation, an average linear heating rate of 2 °C/min ramping to 500 °C was imposed. The heat capacity of the sample was determined from the reversible component, or in-phase component, of the heat flow. Fourier transform infrared spectroscopy (FTIR) was performed using a Thermo Electron Corporation Nicolet 6700 in transmission in the IR wavenumber band 400–4000 cm^{-1} . Sample preparation entailed cogrinding anhydrous potassium bromide and the material of interest at a ratio of 20:1 followed by compression of the resultant mixture in a hand-held International Crystal Laboratories press to form 0.25 in. diameter disks. For analysis of residues resulting from POSS decomposition, 20 mg of virgin POSS was soaked at each temperature of interest in either nitrogen or air in the TGA furnace for 30 min. Because of their hygroscopic nature, resultant residues were kept dry in an oven until further use.

RESULTS

Nonisothermal DSC at a scan rate of 10 °C min^{-1} was utilized to examine the presence of crystallinity in compounds 1–8. Observed melting endotherms and their statistical characteristics are shown in Figure 2. Despite the symmetry of 1, it does

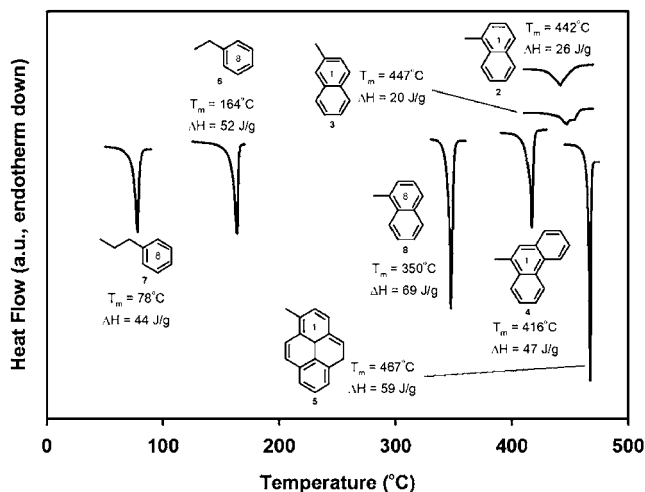


Figure 2. Melting endotherms (standard mode) for compounds 1–8 measured at a heating rate of 10 °C/min. Peak temperatures and corresponding integrated enthalpies are shown.

not exhibit a first order transition between 0 and 500 °C. Broad endotherms of relatively weak intensity were detected for 2 and 3, centered at 442 and 447 °C, respectively. Compounds 4 and 5, on the other hand, despite their asymmetry, exhibit sharp, more intense endotherms characteristic of crystal melting at 416 and 467 °C, respectively. Because this behavior was not immediately intuitive, we revisit these observations in the Discussion. Expectedly, 6 and 7 demonstrate melting endotherms at 164 and 78 °C, respectively. The length of the hydrocarbon bridge between the silicon vertex and the

terminating phenyl group exerts an effect on the observed transitions in that the longer bridge of 7 reduces the energy required for solid–liquid transition. Finally, 8 exhibits a sharp melting endotherm at 348 °C.

Weight loss profiles of symmetric POSS compounds 1 and 6–8 as measured by TGA at a scan rate of 10 °C min^{-1} are plotted in Figure 3 for anaerobic decomposition and in Figure 4

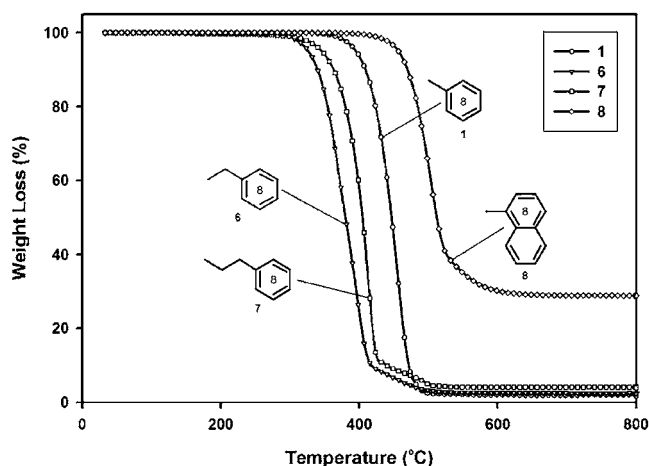


Figure 3. Weight loss profiles for symmetric POSS compounds 1 and 6–8 as a function of temperature under anaerobic conditions (scan rate, 10 °C/min).

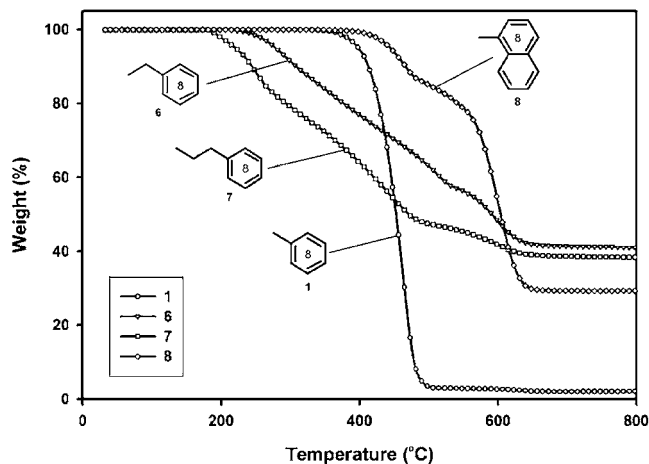


Figure 4. Weight loss profiles for symmetric POSS compounds 6–8 as well as 1 as a function of temperature under aerobic conditions (scan rate, 10 °C/min).

for aerobic decomposition. In an inert atmosphere, weight loss for all compounds proceeds rapidly after initiation and appears to be a predominately single step process prior to mass equilibrium, leaving little ultimate residue at 800 °C, with the exception of 8. As mentioned earlier, 6–8 demonstrate crystal melting transitions by DSC. Therefore, weight loss is likely to occur for these compounds by evaporation dependent on their molecular weights. Accordingly, the temperature at which weight loss is initiated proceeds in the order 6 < 7 < 8. Compound 1 does not fit this trend because it possesses the lowest molecular weight but loses mass at higher temperatures than those witnessed for 6 and 7. Again, no melting point was measured for 1, so it appears that mass loss occurs rapidly after initiation through a sublimative process, commencing at 480

°C. This was confirmed by NMR characterization of condensed sublimate, which indicated structural integrity after volatilization. The remaining substantive residue of **8** at 800 °C, after decomposition, was dark in color. This result suggests at least partial organic character, the occurrence of which may be explained by the relatively high temperature at which the compound boils. Above 500 °C, chemical degradation may dominate over evaporative mass loss, accompanied by a cross-linking process between aromatic groups during carbonization, releasing hydrogen.

In an oxidative atmosphere, the mass loss profile of **1** exhibits no quantitative differences. However, degradation of **6** and **7** begins at 240 and 195 °C, respectively, considerably earlier than observed under anaerobic conditions. Rather than a single rapid weight loss event, loss proceeds in a more gradual, multistep fashion, leaving relatively higher char residues (~40%) at 800 °C due to their comparatively higher degree of intrinsic cage content, which likely converts to SiO₂. Degradation is expected to occur through oxidation of the alkyl spacers between the inorganic core and the exterior phenyl groups. Comparing the lengths of the alkyl spacers of **6** and **7**, the former is more thermally stable due to the shorter methylene bridge between the cage and the phenyl groups. Compound **8** again exhibits mass loss above 400 °C but occurs by a more pronounced two step process with evaporation likely dominating at lower temperature and chemical degradation dominating in the second step at higher temperature.

A parallel analysis of asymmetric POSS compounds 2–5 is presented in Figure 5 for anaerobic and Figure 6 for aerobic

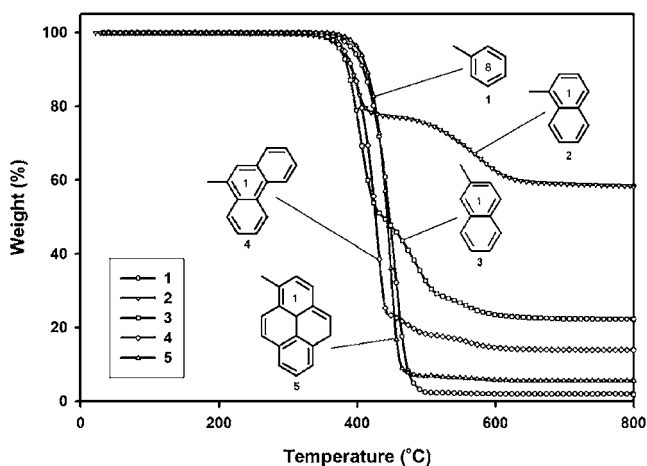


Figure 5. Weight loss profiles for asymmetric POSS compounds 2–5 as well as **1** as a function of temperature under anaerobic conditions (scan rate, 10 °C/min).

decomposition. In an inert atmosphere, mass loss occurs generally via a two-step process. The magnitudes of the initial weight loss event appear in the following descending order: **5** > **4** > **3** > **2**. At first glance, this trend also appears to be a function of the size of the disparate moiety. Although **2** and **3** possess mononaphthyl functionality, which contrasts only in terms of connectivity to the core, the magnitudes of their initial mass loss events differ substantially.

Mass loss profiles for 2–5 and **1** in an oxidative atmosphere are plotted against temperature in Figure 6. Two distinct events are again witnessed for each peripherally asymmetric compound. The distinction between the two events is further

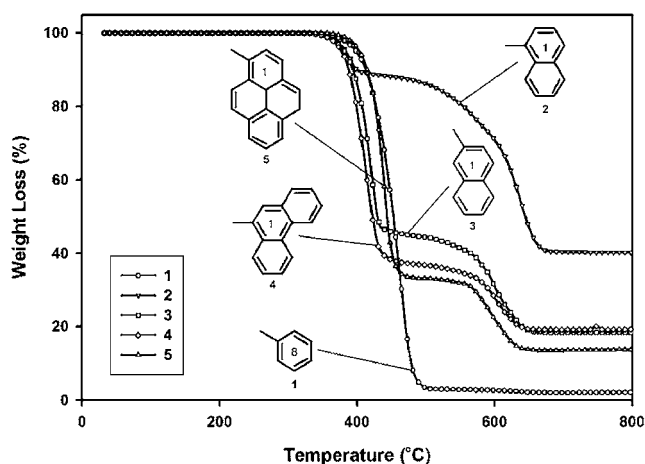


Figure 6. Weight loss profiles for asymmetric POSS compounds 2–5 as well as **1** as a function of temperature under aerobic conditions (scan rate, 10 °C/min).

illustrated in Figure 7, highlighted by mutually exclusive peaks, where the weight loss rate is plotted against temperature. In

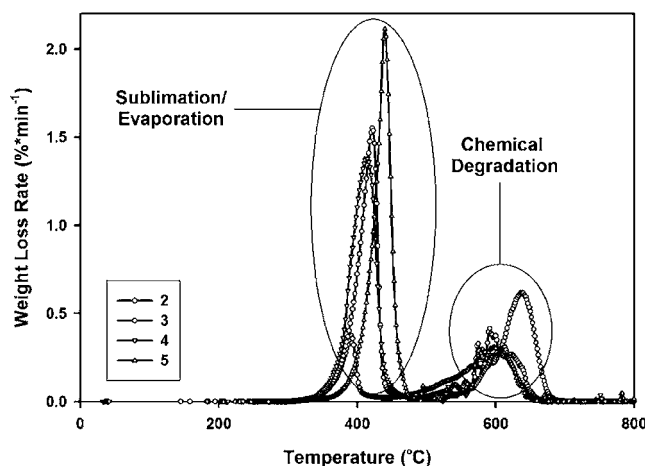


Figure 7. Weight loss rate profiles for asymmetric POSS compounds 2–5 as a function of temperature under aerobic conditions (scan rate, 10 °C/min).

general, the first event is characterized by a high rate of mass loss as a function of temperature (greater profile slope) with a relatively narrow loss rate peak, while the second event is broader, more gradual, and lower in intensity. We postulate here that the first weight loss event is dominated by molecular sublimative or evaporative processes, depending on the phase of the material, and the weight loss of the second event occurring at higher temperatures is largely due to chemical degradation. Comparing anaerobic and aerobic weight loss for the asymmetric POSS compounds, it is evident that the latter environment truncates the first mass loss event perhaps due to oxidative attack in the vicinity of 450 °C. This effect is most pronounced for **4** and **5** and is likely due to the earlier onset of cross-linking reactions concomitant with oxidative attack of hydrogen atoms possessing higher relative reactivity on the phenanthrene and pyrene groups.

Examination of the quantitative details of the mass loss profiles of **1**–**8**, presented in Table 1, provides evidence pertaining to the mechanisms of the mass loss events detected

Table 1. TGA Statistics for POSS Compounds 1–8 after Anaerobic and Aerobic Decomposition

POSS	anaerobic decomposition				aerobic decomposition		
	residue (%)	approx. sub/evap loss (%)	SiO ₂ yield		approx. sub/evap loss (%)	SiO ₂ yield	
			theoretical ^a (%)	experimental (%)		theoretical (%)	experimental (%)
1	1.2	98.8	0.6	0.6	95.2	2.2	1.8
2	58.7	21.7	34.8	34.8	9.8	40.1	40.2
3	14.0	82.0	8.0	7.5	58.5	18.4	18.4
4	21.7	69.0	13.2	14.0	58.0	17.8	19.2
5	8.7	91.1	3.7	6.3	67.0	13.7	13.7
6	2.4	89.9	4.2	2.1	0.0	42.0	41.1
7	4.5	88.7	4.3	4.1	0.0	38.3	38.7
8	28.6	58.9	13.8	16.8	11.6	29.7	29.2

^aTheoretical yield based on oxidation of residual POSS cage content after sublimation/evaporation.

by TGA. In the first set of experiments, the equilibrium product residues from anaerobic decomposition were oxidized to determine POSS cage content, with the assumption that cage loss occurs only during sublimation and evaporation processes and not during chemical degradation, which should proceed through the organic periphery. Theoretical SiO₂ yields for 1–8 after oxidation of the products resulting from anaerobic decomposition were calculated using the following mass balance equation:

$$\text{SiO}_{2,\text{theor}} = (M_i - M_s) \times \frac{416.8 \text{ g/mol}}{\text{MW}} \times 1.15355 \quad (1)$$

where M_i represents initial POSS mass, M_s is POSS mass due to sublimation/evaporation, the factor $416.8 \text{ g mol}^{-1}/\text{MW}$ (POSS molecular weight) represents the weight fraction of SiO_{1.5} in the molecule, and 1.15355 is a constant representing stoichiometric conversion of SiO_{1.5} to SiO₂. Upon comparison, the theoretical SiO₂ yields are in good agreement with those measured after residue oxidation. Imperfect precision for certain compounds is attributed to sublimation/evaporation occurring concurrently with chemical degradation in the late stages of the first mass loss event.

In the second set of experiments, the mass balance eq 1 is applied to the aerobic decomposition processes of 1–8. After correction due to sublimative/evaporative mass loss during the first event, theoretical SiO₂ yields are in more precise agreement with the experimental yields as compared to the anaerobic analysis due to the higher degree of separation between the two mass loss events influenced by oxidation. The hypothesis postulating the mechanisms of the two mass loss events appears to be supported by this analysis.

Further TGA analysis was performed on 2 to elucidate the effects of heating rate on the two distinct events witnessed previously during anaerobic mass loss, the results of which are shown in Figure 8. Five heating rates were imposed on samples possessing equivalent mass (5 mg), that is, 1, 5, 10, 20, and 40 °C min⁻¹. Examination of the peaks of the first derivative functions of the mass loss profiles (rate of weight loss) reveals that with increasing heating rate, the first loss event, dominated by sublimation/evaporation, diminishes in intensity and shifts to higher temperatures. The second mass loss events increase in intensity with heating rate. Compound 2, when exposed to a 1 °C min⁻¹ heating ramp, results in the lowest ultimate char residue, at approximately 40%. Ramps of 5 and 10 °C min⁻¹ expectedly increase the residue mass to above 65% due to a greater role of degradation over sublimation/evaporation. However, this trend does not continue with 20 and 40 °C

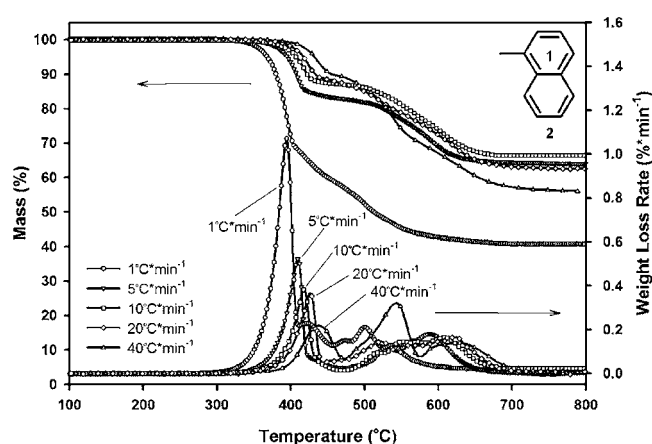


Figure 8. TGA mass loss and mass loss rate profiles of compound 2 at different heating rates under anaerobic conditions.

min⁻¹ heating rates, perhaps due to higher degrees of peripheral group scission from the inorganic core overcoming inter-peripheral chemical reactions.

Mass spectrometry of the gases evolved from anaerobic thermal decomposition of 2 was performed during an imposed heating rate of 10 °C min⁻¹. The relative intensities of m/z ranging from 1 to 199 detected during the temperature sweep are mapped in two-dimensional form in Figure 9. The mass loss and mass loss rate curves are also overlaid on the plot. As stated previously, a mass loss event centered at 400 °C resulting in 20% sample reduction occurs, but no ions outside of the baseline are detected during this event despite its quantitative significance. This observation further substantiates the idea that this event is dominated by sublimation/evaporation. The mass spectrometer is interfaced with the TGA furnace by a long quartz capillary that is heated to a maximum of 190 °C. Intact POSS molecules flowing in the sampling gas stream are expected to condense on the relatively cold walls of the capillary before reaching the ionization current. Over time, this condensation was found to block the capillary restricting achievement of adequate vacuum.

Weak detection of benzene centered at 78 m/z (the signal is magnified through custom software) beginning at ~400 °C during the sweep suggests minute cleavage of phenyl groups from the inorganic core. Signals in the m/z ranges 31, 37–39, 49–52, and 73–79, characteristic of the mass spectrum of benzene, appear in significant intensity during the second mass loss event, further confirming the occurrence of chemical degradation. In addition to benzene, the presence of

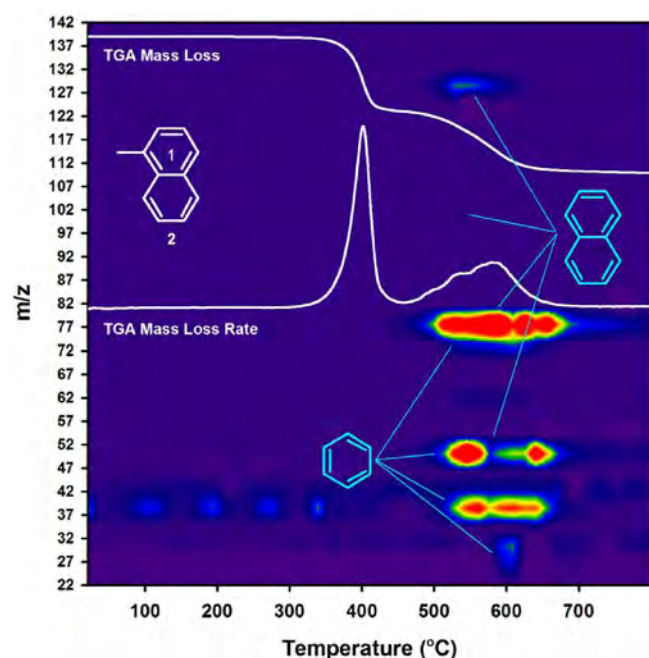


Figure 9. Two-dimensional mass spectrometry representation of the detected intensities of the decomposition products of **2** as a function of TGA furnace temperature. The amu spectrum is 1–199 m/z . The overlay curves are TGA mass loss (above) and mass loss rate (below).

naphthalene is also detected, although of expectedly weaker intensity due to its mass fraction in **2**, as evidenced by m/z detection in the ranges of 61–64, 98–103, and 126–129. Detection of benzene in the m/z 73–79 is also expected due to naphthalene decomposition in the ionization current but only increases the intensity of m/z detected in that region for benzene originating from cleavage of phenyl groups.

To explore thermally induced degradation of POSS in the solid state, FTIR was employed to study the evolution of **2** during heat treatment at various temperatures in both nitrogen and air. Unique samples were exposed to a prescribed temperature and atmosphere until mass equilibrium was achieved (generally ~ 10 min) in the TGA furnace. The resulting residues were coground with KBr, pelletized, and analyzed in terms of IR wavelength absorbance.

Photographs of the samples in their pans subsequent to heat treatment in nitrogen are shown in Figure 10, adjacent to their corresponding FTIR absorption spectra. The material appears unchanged after treatment at 300 °C and appears to have flowed and consolidated after exposure to 400 °C. An amber discoloration transpires during the 600 °C soak, followed by substantial darkening during exposure to the final two temperatures. Key absorption bands are labeled on the spectra corresponding to virgin **2**. From highest to lowest wavenumber, these bands as labeled in the figure include (1) C–H phenyl asymmetric stretching at 3050 cm^{-1} , (2) aromatic C=C asymmetric stretching at 1600 cm^{-1} , (3) Si-phenyl deformation at 1137 and 1432 cm^{-1} , (4) Si–O deformation at 1100 cm^{-1} , (5) aromatic C–H bending at 700 cm^{-1} , and (6) Si–O–Si out-of-plane bending at 500 cm^{-1} . No changes are detected in the spectra of **2** after annealing at 400 °C in comparison with the spectra of virgin material. A gradual attenuation of the bands corresponding to Si-phenyl deformation takes place, with increasing temperature until a peak is no longer witnessed at 1432 cm^{-1} after 700 °C. The peak corresponding to aromatic

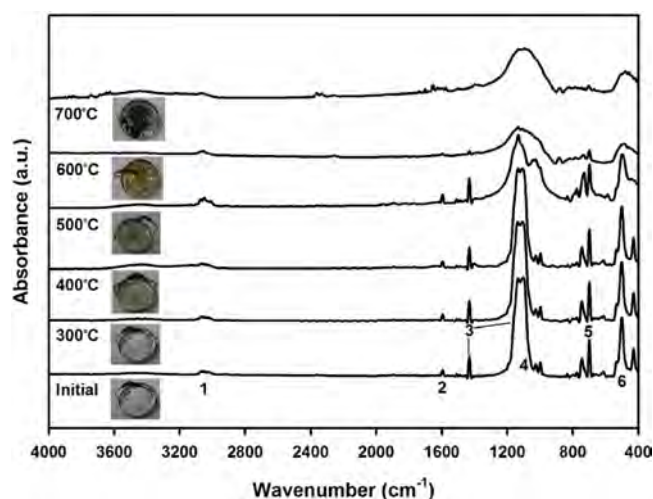


Figure 10. FTIR spectra of **2** after heat treatment for 30 min at increasing temperatures in anaerobic conditions. A new sample was used for each heat treatment experiment.

C=C stretching broadens, while the peaks attributed to aromatic C–H bending and stretching diminish in intensity with increasing soak temperature. Finally, the peaks originating from Si–O cage deformation and Si–O–Si out-of-plane bending broaden significantly, suggesting loss of cage integrity and formation of an amorphous Si–O lattice structure. The evolution of the organic peaks also suggests that free aromatic carbonaceous material exists in the char residue after the 700 °C soak. TGA analysis revealed that $\sim 25\%$ of the char residue is organic in character.

Analogous information pertaining to heat treatment of **2** in air at different temperatures is offered in Figure 11. In this case,

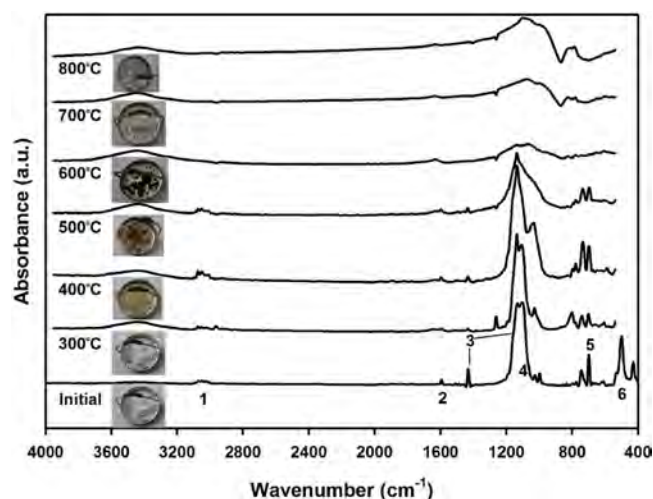


Figure 11. FTIR spectra of **2** after heat treatment for 30 min at increasing temperatures in air. A new sample was used for each heat treatment experiment.

the powder again flows and consolidates between 300 and 400 °C. However, in this case, discoloration occurs earlier at 400 °C, with gradual darkening occurring to 600 °C. Above this temperature, the residue is completely white, insinuating pure SiO_2 . In air, absorbance peaks 1–3 and 5, resulting from the organic fraction, diminish in intensity to 600 °C, after which peaks attributed to absorption of SiO bonds in silicon dioxide,

including the stretching mode at 1070 cm^{-1} , a rocking mode at 450 cm^{-1} , and a bending mode at 810 cm^{-1} , appear and increase in intensity. At and above $700\text{ }^{\circ}\text{C}$, there is no evidence of absorption by organic bonds in the residue.

On the basis of the FTIR spectra, it appears that thermal decomposition of **2** occurs primarily through homolytic cleavage of the phenyl–silicon and naphthyl–silicon bonds. The fate of cleaved aromatic radicals depends on the atmosphere. In an inert environment, cleaved radicals can react with each other to form a carbonaceous phase, which ultimately remains in the char, while other radicals through proton abstraction form gaseous benzene and naphthalene, which was strongly detected during the second TGA mass loss event as measured by mass spectrometry. In an oxidizing atmosphere, on the other hand, aromatic radicals are completely oxidized evacuating the pyrolyzing residue in the gaseous phase. The remaining SiO is converted to SiO_2 as suggested by the quantitative mass balance treatment of the TGA data as well as the FTIR spectra.

The dependence of molar specific heat capacity (C_n) on temperature for **1**–**8**, measured by MDSC, is plotted in Figure 12 in the range 20 – $100\text{ }^{\circ}\text{C}$. Results were consistent across four

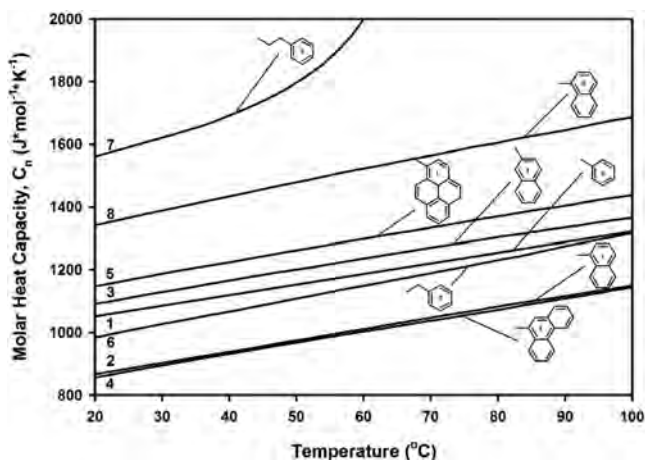


Figure 12. Molar heat capacities (C_n) for compounds **1**–**8** plotted against temperature determined from the reversible component of MDSC.

runs using different samples. Specific heat capacities at $25\text{ }^{\circ}\text{C}$ range from $0.81\text{ J g}^{-1}\text{ K}^{-1}$ for **4** to $1.27\text{ J g}^{-1}\text{ K}^{-1}$ for **7**. These values are expectedly greater than that of fused silica ($0.70\text{ J g}^{-1}\text{ K}^{-1}$) due to the POSS core structure and organic periphery, which compromise atom density in relation to SiO_2 . Molar heat capacities range from 860 to $1560\text{ J mol}^{-1}\text{ K}^{-1}$ for **4** and **7**, respectively. Overall, the nature of the periphery appears to play a significant role due to the observed variation in C_n .

For the symmetric POSS compounds, **7** demonstrates the highest heat capacity across the given temperature range, followed in descending order by **8**, **1**, and **6**. The slopes of **6** and **7** are noticeably greater than those of the other compounds, and these materials are differentiated by the presence of alkyl spacers between the inorganic core and the peripherally terminating phenyl groups. The flexibility in these spacers results in a greater dependence of heat capacity on temperature due to an additional thermally activated peripheral group bending mode beyond only the pure rotation available to the other aryl groups.

For the asymmetric compounds, **3** and **5** exhibit the highest heat capacities and are relatively similar across the entire temperature range, with that of **5** being greater. In contrast, the molar heat capacities of **2** and **4** demonstrate the lowest molar heat capacities of all eight compounds and are nearly identical. An explanation is presented in the next section.

To ascertain the geometric effects of the aryl periphery on POSS assembly, XRD was conducted. The objective of single-crystal XRD was to discern atomic packing fractions and theoretical densities, while powder XRD was used to determine average cage-to-cage distances. To clarify, powder XRD was performed on materials representative of their morphological states after synthesis, which were likewise used for thermal characterization. Only substantive stable crystals of **1**, **4**, **5**, and **8** were successfully solution grown. Their crystal structures were resolved and will be described in greater detail in a forthcoming paper. All demonstrate triclinic unit cells. As expected, increasing the size of aryl group increases unit cell volumes as shown in Table 2. Additionally, Table 1 presents the

Table 2. Statistics for the Unit Cells Determined from Single-Crystal XRD of the POSS Compounds That Yielded Stable, Solution Grown Crystals

POSS	$V\text{ (}\text{\AA}^3\text{)}$	Z	with solvent		solvent removed	
			$\rho\text{ (g cm}^{-3}\text{)}$	APF	$\rho\text{ (g cm}^{-3}\text{)}$	APF
1 (C_6H_{12})	1390	1	1.24	0.82	1.24	0.79
4 (CHCl_3)	3041	2	1.42	0.82	1.24	0.79
5 (THF)	3208	2	1.29	0.92	1.20	0.76
8 (THF)	3983	2	1.25	0.91	1.20	0.78

theoretical density values obtained from the Mercury software, as well as the atomic packing factors (APFs) calculated based on the simplifying assumption that each atom within the unit cell occupies $1\text{ }\text{\AA}^3$. The unit cells of these four compounds revealed the presence of solvent molecules in all cases. However, the number of solvent molecules within the unit cells varied because the size and distribution of regions of free volume contrasted for the four crystal structures. Because the single-crystal structures may not represent the states of the POSS molecules resulting from their syntheses and to gain further information, two cases are presented in Table 2. The theoretical densities and APFs are reported for the resolved unit cells containing solvent and with the solvent molecules removed. With solvent present, the APFs for **5** and **8** are artificially greater than that of **1** and **4** due to the greater number of solvent molecules present in the latter two. However, when only the atoms pertaining to the POSS molecules are considered in the calculations, the APFs and theoretical densities are quite similar for all four compounds.

Further qualitative examination of the crystal packing of **1**, **4**, **5**, and **8** reveals the presence of attractive aromatic interactions between adjacent molecules. Schematics of these interactions extracted from the expanded crystal packing of the unit cells of **1**, **4**, and **8** are depicted in Figure 13. For **1**, two types of interactions are prevalent, characterized by both offset parallel and T-shaped stacking beyond the van der Waals radius of carbon. These range in atomic distance between 3.65 and $3.90\text{ }\text{\AA}$, which is less than that experimentally found for benzene dimers in the gas phase.³¹ Compound **8** exhibits only offset parallel interactions between a fraction of the 1-naphthyl moieties at distances between 3.28 and $3.36\text{ }\text{\AA}$. For **4**, phenanthrene groups from adjacent POSS molecules also

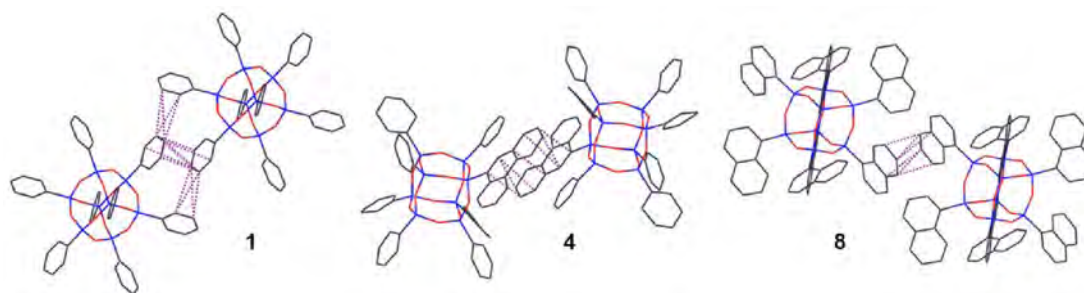


Figure 13. Schematics of aromatic interactions between adjacent POSS molecules extracted from the unit cell crystal packing of **1** (left), **4** (center), and **8** (right). Atoms are color coded as follows: Si (blue), O (red), and C (charcoal). Hydrogen atoms are omitted for clarity.

participate in offset parallel interactions at a consistent distance of 3.5 Å, while no other aromatic interactions between the majority phenyl groups are evident. The overall packing and locations of pyrenyl groups for **5** are similar to **4** (illustration not shown) with weak short-range interactions between the pyrenyl groups occurring at slightly greater distances than those witnessed in **4**. The relatively high degree of aromatic interactions observed in the molecular packing structure of **1** likely contributes to the high macroscopic binding energy of its crystals prevalent in its commercial form.

Powder XRD spectra for **1–5** and **8** as a function of Bragg angle 2θ and corresponding d -spacings are shown in Figure 14.

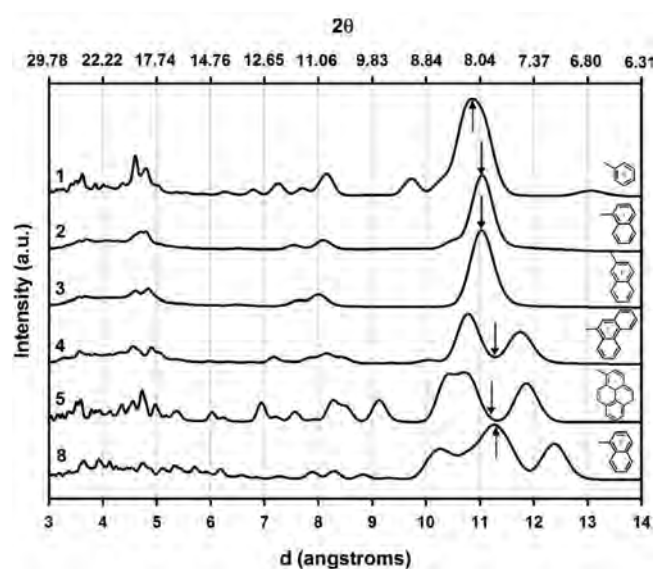


Figure 14. Powder XRD spectra for compounds **1–5** and **8** as a function of d -spacing and 2θ . The arrows indicate averaged cage-to-cage distance calculated from the relevant scattering peaks.

Each compound demonstrates semicrystalline behavior due to the appearance of scattering peaks, which are somewhat broad due to the efficiency of the detector, but are nonetheless distinct. Peaks of highest intensity are located in the region between 6 and 10°. Scattering in this region emanates from electron density periodicity corresponding to the distance between the faces of adjacent POSS cages. Transformation of the 2θ to distance reveals a broad peak centered at 10.8 Å for **1**, in agreement with the averaged principal unit cell axes a and c observed from single-crystal XRD, and 12.4 Å for **8**, also in agreement with the averaged principal unit cell axes a and b . Because of limitations of the detector, scattered radiation

emanating from electron periodicity in the c -axis for **8** at 16.35 Å cannot be resolved. However, a peak with maximum at 13 Å for **1** may be attributed to periodicity along the b crystallographic direction. The two scattering peak maxima for **4**, located at 10.77 and 11.73 Å, are not in as good agreement with the a - and b -axes, possibly due to different crystal forms manifested during synthesis, as opposed to those from the longer, more controlled solution conditions that were used to generate single crystals. This discrepancy may arise from kinetic effects of molecular asymmetry during assembly. Likewise, for **5**, only scattering intensity corresponding to periodicity along the b -axis is in agreement with that determined from single-crystal XRD.

Comparison of the peaks corresponding to assumed average cage-to-cage distances for **1–5** and **8**, based on this analysis, reveals a trend. Arrows indicating averages are also shown in Figure 14. As expected, **1** exhibits the shortest average cage-to-cage distance, while that of **8**, whose structure possesses 1-naphthyl groups at every silicon vertex, demonstrates the largest. Examination of the spectra collected from corner-capped compounds **2–5** further elucidates a relationship between the averaged cage-to-cage distance and the geometric size of the corner cap: 1-pyrenyl \sim 9-phenanthrenyl $>$ 2-naphthyl \sim 1-naphthyl.

DISCUSSION

Solid–liquid transition determination for compounds **1–5** by standard DSC revealed intriguing results. Specifically, that **1**, despite its symmetry, did not exhibit a melting point, while asymmetric compounds **4** and **5** conversely showed strong, sharp transitions above 400 °C. Characterization of these compounds was performed on powder in states resulting from their syntheses. During the product isolation step, POSS–THF solutions were slowly added dropwise to methanol to promote precipitation. POSS assembly is expected to be quite rapid during this process, resulting in local regions containing amorphous, crystalline, or semicrystalline character. Because of the propensity for the phenyl groups of **1** to participate in aromatic interactions as elucidated by single-crystal XRD, it is possible that this interplay impedes a high degree of cage ordering during precipitation. Referring back to Figure 14, strong X-ray scattering peaks in the spectra for **1** in the d -spacing range of 3.5–4 Å support the presence of aromatic stacking interactions in powder form. Alternatively, the observance of both T-shaped and parallel displaced aromatic interactions, combined with efficient POSS packing, may result in crystal binding energy that prevents a solid–melt transition from occurring prior to thermally induced degradation. This is less likely because **1** appears to completely sublime rapidly at

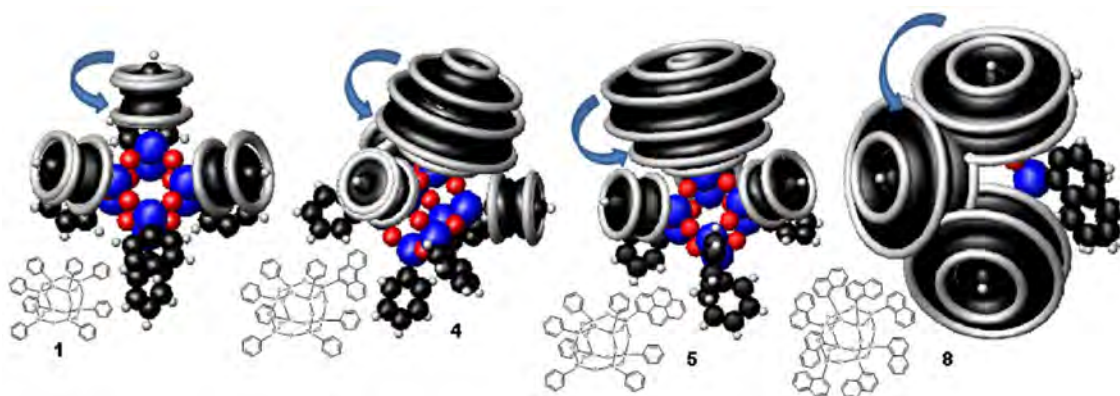


Figure 15. Graphical representation of thermally induced peripheral group rotation for 1, 4, 5, and 8, illustrating required volume occupation of neighboring chemical moieties. The atom locations were obtained from single-crystal XRD.

~400 °C, according to TGA. The sharp melting endotherms corresponding to asymmetric compounds 4 and 5 are also not intuitive. Enhanced crystallization of these compounds may be attributed to the larger corner groups, which may guide the formation of enhanced crystallinity due to their higher potential for genuine π - π interactions, recently computationally shown to occur for aromatic ring structures containing 11 or more carbon atoms.³² This phenomenon is further supported by recalling that 2 and 3 exhibited relatively weak melting endotherms, as compared to 4 and 5. Also noteworthy, the compounds that exhibit sharp endotherms by DSC demonstrate multiple peaks in their X-ray scattering spectra in the d -spacing range of 10–13 Å, likely indicating a higher degree of three-dimensional order.

The mass loss profiles by TGA in nitrogen, as well as the measured molar heat capacities of all of the studied compounds, illustrated surprisingly contrasting behaviors of compounds 1–5, despite possessing similar peripheries. Again, rapid sublimation of 1 may be explained by a lack of significant crystallinity as discussed previously. Compounds 2 and 3 each possess naphthyl corner caps, differing only in their isomeric connectivity to the core. The magnitude of the first volatilization mass loss events and coincidentally the molar heat capacity of 3 are much greater than those of 2. Increasing the temperature of POSS is expected to induce excitation of the peripheral groups. For most of the compounds studied, the majority of aryl groups possess only one degree of freedom in terms of their ability for motion, namely, rotation about the covalent Si–C bond. Compounds 6 and 7, due to the presence of alkyl spacers between the cage and the exterior phenyl groups, retain an additional degree of freedom due to their ability to translate in three-dimensional space. During thermal excitation, the rotational inertia is greater for moieties of higher molecular mass but is also dependent on the squared distance of molecular mass from the axis of rotation. On the basis of these principals, the rotational inertia of the 1-naphthyl group in 2 should be greater than those of 2-naphthyl in 3 and similar to 9-phenanthrenyl in 4. The measured molar heat capacities do not reflect this assumption. Compounds 2 and 4 exhibit similar molar heat capacities, which are relatively low, and their corner-cap groups possess the same type of connectivity to the core. This connectivity is expected to limit rotation due to electronic density barriers imposed by surrounding phenyl groups. Therefore, the heat capacities of 2 and 4 are relatively low due to sterically influenced excitation of the corner-capping groups. Compounds 3 and 5, on the other hand, display

relatively high heat capacity values. In this case, because of the similar nature of the connectivity of the 2-naphthyl and 9-pyrenyl groups to the core, these groups should have lower barriers to rotation and therefore be susceptible to greater excitation, resulting in higher heat capacities. The heat capacity of 5 is expectedly greater than that of 3 due to the higher molar mass of the pyrenyl group with a similar mass radius relative to the axis of rotation. This theory appears to explain the magnitudes of the heat capacities for the remaining compounds, with 1 exhibiting a greater heat capacity than 2 and 4, because all phenyl groups can rotate during excitation, but less than 3 and 5 due to the greater molar masses of their corner-cap groups. Compound 8 expectedly demonstrates a greater heat capacity than 5, while 7 exhibits the highest heat capacity due to its additional degree of translational freedom. An illustration of peripheral group rotation for 1, 4, 5, and 8 is shown in Figure 15, where associated volumes resulting from revolution are shown. The close proximities of the objects resulting from group rotation in 4, 5, and 8 are expected to result in sterically limited rotation or the necessity for cooperative rotational motion between the neighboring groups.

We extend this theory to the observed TGA mass loss profiles of 2–5. Thermally induced rotational excitation of the peripheral groups requires volume. As such, the size of the volumetric ellipsoid created by group rotation is dictated by the geometry and connectivity of the involved group as well as local steric effects. Therefore, geometrically larger aryl peripheries should increase the propensity for the molecule to escape by sublimation/evaporation during heating, since free volume development concomitant with thermally induced excitation is expected to be greater. This theory could explain the contrast in first event mass losses between 2 and 3 despite their similarities in functionality. The greater potential degree of corner-cap excitation and associated spatial requirements of the 2-naphthyl moieties relative to 1-naphthyl groups could contribute to a higher propensity for thermally initiated evaporation/sublimation. In this case, the nature of the connectivity is postulated to affect rotational potential.

The exception to this theory is the mass loss profile of 8. To further study this, we revisit our TGA results. Figure 16 presents data pertaining to 10 wt % decomposition temperatures by TGA, as a function of POSS periphery and molecular weight, for a wide range of POSS molecules, including those that are the focus of this study. The aliphatic POSS data used to assimilate this plot originate from Fina et al.¹⁹ and Bolln et al.²¹ and, to some extent, has been reproduced with similar results in

our laboratory. Compounds featuring peripheries consisting of hydrogen, methyl, and ethyl groups, respectively, undergo complete sublimation at increasing temperature with molecular weight. No phase transitions are detected for these materials by DSC. Contrastingly, POSS molecules with alkyl peripheries of 3–9 carbon atoms in length undergo mass loss via evaporation above their melting points. Ten percent mass loss temperatures (designated by the variable T_{d10}) for these compounds follow a trend fitted to a second order polynomial with $R^2 = 0.99$, proceeding accordingly with increasing molecular weight. Overall, POSS crystallization is facilitated by alkyl group size due to an increasing propensity for peripheral interactions and alignment with increasing chain length. Sublimative and evaporative mass losses are dictated by molecular weight, with higher mass requiring more energy to volatilize.

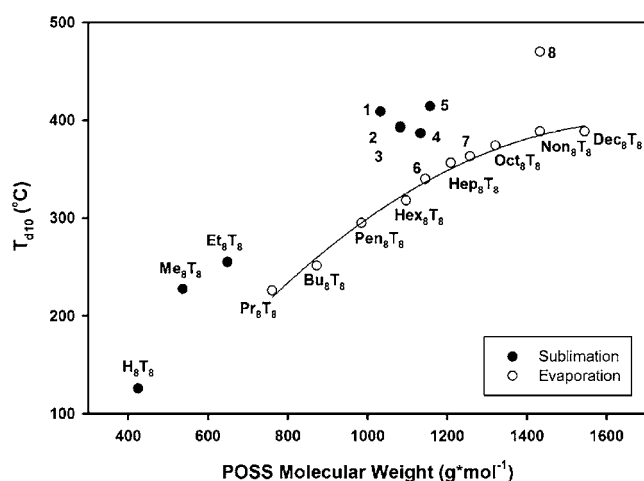


Figure 16. Ten percent mass loss temperatures as a function of molecular weight for POSS featuring aliphatic, aromatic, and hybrid peripheries incrementing in size. The aliphatic POSS data used to calculate the polynomial curve fitting in the assimilated plot originate from [20] and [22]. The nomenclature R_8T_8 indicates a cubic Si_8O_{12} core with eight T type Si atoms, surrounded by a symmetric periphery consisting of R groups.

For the aryl POSS compounds, 6 and 7 fall on the second order polynomial determined from T_{d10} values for the peripherally aliphatic compounds. Compound 8, on the other hand, does not fall on this curve despite demonstrating a melting point at 348 °C. This outlying behavior could be due to adjacent molecule peripheral interactions between 1-naphthyl groups suppressing more substantial volatility prior to chemical degradation. Corner-capped compounds 1–5, as presented earlier, undergo an initial mass loss event characterized by sublimation or evaporation. These compounds also do not fall on the fitted polynomial but are clustered together exhibiting similar T_{d10} values for their calculated molecular weights. Classification of purely aryl POSS compounds using this methodology likely has little meaning due to their complex interactions, mass loss behavior, and relative thermal stability.

SUMMARY

Investigation of the molecular packing and thermal properties of eight aryl-functionalized POSS compounds revealed that despite possessing structurally similar peripheries in most cases, the geometry of the organic corona profoundly influences crystallization behavior, thermally induced mass loss and

degradation, and interactions between neighboring molecules. Interestingly, although the periphery was found to affect unit cell dimensions resolved from the XRD of single crystals, APFs and theoretical densities were calculated to be similar in the absence of solvent molecules. Solution-born crystals were found to derive structural stability with solvent molecules contained within the unit cells, their location and population dictated by free volume distribution. Multiple types of aromatic interactions were observed and are postulated to guide crystallization for peripheral groups exceeding a threshold carbon content, such as those of phenanthrene and pyrene. In this case, genuine π – π interactions appear to facilitate nonintuitive assembly of peripherally asymmetric POSS compounds, leading to the observation of intense solid–liquid transitions. In presumably less ordered synthetic powders, the geometry of the periphery affects averaged cage-to-cage distances. TGA revealed that mass loss is affected by both peripheral architecture and atmospheric environment. In most cases, mass loss is shown to occur via a two step process, which is generally accelerated in an oxidative environment. Through the application of a mass balance technique, loss was shown to proceed through volatilization processes in the first step, while at higher temperatures, chemical degradation was determined to be the dominant mechanism. TGA-interfaced mass spectrometry revealed that purely aryl POSS compounds, in an inert atmosphere, are principally chemically robust to ~ 500 °C, where scission of organic groups from the core is the prevalent degradation mechanism. POSS molecules possessing alkyl spacers between their core and phenyl groups exhibit relatively low melting points at the expense of thermal stability. A complex dependence of measured molar heat capacity on peripheral architecture was also uncovered. This may be influenced by the nature of peripheral group connectivity to the POSS cage, as well as available degrees of freedom and required rotational inertia for thermally activated peripheral group excitation. Our results suggest that peripheral group rotation significantly influences the heat capacity and volatility of assembled POSS molecules in the solid state. Finally, aryl POSS compounds were found to exhibit more complicated mass loss behavior than their alkyl counterparts, which generally boil according to their molecular weights. This complex behavior is attributed to aromatic interactions between POSS molecules coupled with their relatively high thermal stability.

AUTHOR INFORMATION

Corresponding Author

*Tel: +1-661-275-5943. E-mail: gregory.yandek@edwards.af.mil (G.R.Y.). Tel: +1-661-275-5857. E-mail: joseph.mabry@edwards.af.mil (J.M.M.).

Notes

The authors declare no competing financial interest.

ACKNOWLEDGMENTS

We gratefully acknowledge financial support from the Air Force Office of Scientific Research and the Rocket Propulsion Division of the Air Force Research Laboratory. We also thank Dr. Andrew Guenther, Dr. Timothy Haddad, and Prof. Andre Lee for insightful discussions.

REFERENCES

- (1) POSS is a registered trademark of Hybrid Plastics, I, Hattiesburg, MS.

- (2) Ghanbari, H. C.; Brian, G.; Seifalian, A. M. *Macromol. Rapid Commun.* **2011**, 32 (14), 1032–1046.
- (3) DeArmitt, C.; Wheeler, P. *Plast. Addit. Compd.* **2008**, 10 (4), 36–39.
- (4) Soh, M. S.; Sellinger, A.; Yap, A. U. J. *Curr. Nanosci.* **2006**, 2 (4), 373–381.
- (5) Joshi, M. B.; Singh, B. J. *Macromol. Sci., Polym. Rev.* **2004**, C44 (4), 389–410.
- (6) Phillips, S. H. H.; Timothy, S.; Tomczak, S. J. *Curr. Opin. Solid State Mater. Sci.* **2004**, 8 (1), 21–29.
- (7) Nguyen, T. P.; Lee, C. W.; Hassen, S.; Le, H. C. *Solid State Sci.* **2009**, 11 (10), 1810–1814.
- (8) Wu, M.; Wu, R.; Zhang, Z.; Zou, H. *Electrophoresis* **2011**, 32 (1), 105–115.
- (9) Madbouly, S. A.; Lendlein, A. *Adv. Polym. Sci.* **2010**, 226, 41–95.
- (10) Bourbigot, S. D.; Jama, C. *Macromol. Symp.* **2006**, 233 (Fillers, Filled Polymers and Polymer Blends), 180–190.
- (11) Chhatre, S. S.; Tuteja, A.; Choi, W.; Revaux, A.; Smith, D.; Mabry, J. M.; McKinley, G. H.; Cohen, R. E. *Langmuir* **2009**, 25 (23), 13625–13632.
- (12) Lickiss, P. D.; Rataboul, F. *Adv. Organomet. Chem.* **2008**, 57, 1–116.
- (13) Misra, R.; Alidedeoglu, A. H.; Jarrett, W. L.; Morgan, S. E. *Polymer* **2009**, 50, 2906–2918.
- (14) Tanaka, K.; Adachi, S.; Chujo, Y. *J. Polym. Sci., Part A: Polym. Chem.* **2009**, 47, 5690–5697.
- (15) Yen, Y.-C.; Kuo, S.-W.; Huang, C.-F.; Chen, J.-K.; Chang, F.-C. *J. Phys. Chem. B* **2008**, 112 (35), 10821–10829.
- (16) Lim, S.-K.; Hong, E.-P.; Choi, H. J.; Chin, I.-J. *J. Ind. Eng. Chem.* **2010**, 16 (2), 189–192.
- (17) Pracella, M.; Chionna, D.; Fina, A.; Tabuani, D.; Frache, A.; Camino, G. *Macromol. Symp.* **2006**, 234, 59–67.
- (18) Fina, A.; Tabuani, D.; Frache, A.; Camino, G. *Polymer* **2005**, 46, 7855–7866.
- (19) Fina, A.; Tabuani, D.; Carniato, F.; Frache, A.; Boccaleri, E.; Camino, G. *Thermochim. Acta* **2006**, 440, 36–42.
- (20) Mantz, R. A.; Jones, P. F.; Chaffee, K. P.; Lichtenhan, J. D.; Gilman, J. W. *Chem. Mater.* **1996**, 8, 1250–1259.
- (21) Bolln, C.; Tsuchida, A.; Frey, H.; Mulhaupt, R. M. *Chem. Mater.* **1997**, 9, 1475–1479.
- (22) Blanco, I.; Abate, L.; Bottino, F. A.; Bottino, P.; Chiacchio, M. A. *J. Therm. Anal. Calorim.* **2012**, 107 (3), 1083–1091.
- (23) Brook, M. A. *Silicon in Organic, Organometallic, and Polymer Chemistry*, 2000 ed.; John Wiley & Sons: New York, 2000; p 30.
- (24) Cottrell, T. L. *The Strengths of Chemical Bonds*, 2nd ed.; Butterworths: London, 1958.
- (25) Chen, J.-H.; Yao, B.-X.; Su, W.-B.; Yang, Y.-B. *Polymer* **2007**, 48 (6), 1756–1769.
- (26) Kopesky, E. T.; McKinley, G. H.; Cohen, R. E. *Polymer* **2006**, 47, 299–309.
- (27) Bourbigot, S.; Le Bras, M.; Flambard, X.; Rochery, M.; Devaux, E.; Lichtenhan, J. D. Polyhedral oligomeric silsesquioxanes: Application to flame retardant textiles In *Fire Retardancy of Polymers: New Applications of Mineral Fillers*; Le Bras, M., Ed.; European Meeting on Fire Retardancy and Protection of Materials: Lille, France, 2005; Vol. 9, pp 189–201.
- (28) Moore, B. M.; Ramirez, S. M.; Yandek, G. R.; Haddad, T. S.; Mabry, J. M. *J. Organomet. Chem.* **2011**, 696 (13), 2676–2680.
- (29) Feher, F. J.; Budzichowski, T. A. *J. Organomet. Chem.* **1989**, 373 (2), 153–163.
- (30) Olsson, K.; Gronwall, C. *Ark. Kemi* **1960**, 28, 529–540.
- (31) Sinnokrot, M. O.; Valeev, E. F.; Sherrill, C. D. *J. Am. Chem. Soc.* **2002**, 124 (36), 10887–10893.
- (32) Grimme, S. *Angew. Chem., Int. Ed.* **2008**, 47 (18), 3430–3434.